SAND2020-2681C

ARMA 20-1590

# Initial Simulations of Empty Room Collapse and Reconsolidation at the Waste Isolation Pilot Plant

Benjamin Reedlunn[1], Georgios Moutsanidis[2], Jonghyuk Baek[3], Tsung-Hui Huang[3], Jacob Koester[1], Xiaolong He[3], Haoyan Wei[3,4], Karan Taneja[3], Yuri Bazilevs[5], and Jiun-Shyan Chen[3]

[1] *Sandia National Laboratories, Albuquerque, New Mexico, USA*
[2] *Stony Brook University, Stony Brook, New York, USA*
[3] *University of California San Diego, La Jolla, California, USA*
[4] *Livermore Software Technology, ANSYS, Livermore, California, USA*
[5] *Brown University, Providence, Rhode Island, USA*



**ABSTRACT:** Room ceilings and walls at the Waste Isolation Pilot Plant tend to collapse over time, causing rubble piles on floors of empty rooms. The surrounding rock formation will gradually compact these rubble piles until they eventually become solid salt, but the length of time for a rubble pile to reach a certain porosity and permeability is unknown. This paper details the initial model development to predict the porosity and fluid flow network of a closing empty room. Conventional geomechanical numerical methods would struggle to model empty room collapse and rubble pile consolidation, so three different meshless methods, the Immersed Isogeometric Analysis (IGA) Meshfree Method, Reproducing Kernel Particle Method (RKPM), and Conformal Reproducing Kernel (CRK) method, were assessed. First, each meshless method simulated gradual room closure, without ceiling or wall collapse. All methods produced equivalent predictions to a finite element method reference solution, with comparable computational speed. Second, the Immersed IGA Meshfree method and RKPM simulated two-dimensional empty room collapse and rubble pile consolidation. Both methods successfully simulated large viscoplastic deformations, fracture, and rubble pile rearrangement to produce qualitatively realistic results. Finally, the meshless simulation results helped identify a mechanism for empty room closure that had been previously overlooked.

## 1 INTRODUCTION

The Waste Isolation Pilot Plant (WIPP) is a geologic repository for defense-related nuclear waste. If left undisturbed, the virtually impermeable rock salt surrounding the repository will isolate the nuclear waste from the biosphere. If humans accidentally drill a borehole through the repository, as well as a hypothetical brine pocket beneath the repository, then the likelihood of a radionuclide release to the biosphere will depend significantly on the porosity and permeability of the repository itself. If the permeability is nonexistent, then brine will only flood the immediate vicinity of the borehole and transport a small to negligible amount of radionuclides to the biosphere. If brine can freely flow throughout the repository, then a larger radionuclide release will be possible. The repository's porosity also is important. A small fluid storage volume coupled with a large amount of brine and gas will lead to high pressures. Higher pressures can potentially drive brine and gas into regions of low permeability, and/or up a borehole to the earth's surface.

Sandia has models for the permeability and porosity of rooms filled with waste containers and crushed salt (Stone, 1997; Camphouse et al., 2012). Although these filled room models have areas for improvement, they are based on science and engineering judgement. Sandia, on the other hand, does not have a model for the permeability and porosity of empty rooms as they close.

Room ceilings and walls at the WIPP tend to collapse over time, while room floors tend to slowly

Sandia National Laboratories is a multimission laboratory managed and operated by National Technology & Engineering Solutions of Sandia, LLC, a wholly owned subsidiary of Honeywell International Inc., for the U.S. Department of Energy's National Nuclear Security Administration under contract DE-NA0003525.

heave, because salt cracks when exposed to shear stress without sufficient confining pressure. Cracks form in the excavation damaged zone (EDZ), also known as disturbed rock zone (DRZ), near the room due to the lack of stiff support (confining pressure). These cracks can lead to blocks of salt detaching from the surrounding rock formation. When blocks detach around filled rooms, Sandia has historically assumed the room contents support these blocks enough that the blocks still mate up with the surrounding rock formation as the room closes. When blocks detach around empty rooms, however, the blocks can fall several meters, land on the floor, and possibly break into smaller pieces, as shown in Fig. 1.

(a) Lower horizon rubble pile in Panel 7, Room 4 (November, 2016)

(b) Upper horizon rubble pile in E300-S3650 access drift (September, 2016)

Figure 1: Photographs of rubble piles resulting from roof falls at the WIPP (Carrasco, 2019b).

The U.S. Department of Energy, at the recommendation of Nuclear Waste Partnership, LLC, the managing and operating contractor at WIPP, has decided to abandon several parts of the WIPP, rather than fill them full of waste or crushed salt, due to operational safety concerns (Carrasco, 2019a). This decision raises the question, "How do the permeability and porosity of an empty room evolve over time?" The rubble piles in Fig. 1 undoubtedly have numerous flow pathways and gas storage sites. How much time will pass before the surrounding rock formation compresses a rubble pile to its final state?

This paper focuses on room collapse and rubble pile reconsolidation. Another part of the project is using computational fluid dynamics to predict the permeability of the rubble pile (see Chapter 7 in Reedlunn et al., 2019). Eventually, the flow simulations will likely use the flow network geometry predicted by the rubble pile reconsolidation simulations.

Room collapse and reconsolidation involve several complex processes. The driving force for room closure is the weight of the overburden coupled with salt's viscoplasticity, but smooth viscoplastic closure without fractures is different than closure with fractures. First, fracturing around a room will likely cause square or rectangular room cross-sections to transition to more circular cross-sections. Circular cross-sections viscoplastically close more slowly than other two-dimensional shapes because circular cross-sections distribute the stress around a room more evenly. Second, fracturing often results in rubble piles. A rubble pile will supply back pressure to the surrounding rock formation, which reduces the deviatoric stress in the surrounding rock and slows down the rate of room closure. The amount of back pressure supplied by the rubble pile will depend on how big the rubble pieces are, as well as how easily they rearrange, fracture, and heal.

Predicting room collapse and reconsolidation will be a challenging endeavor. As just discussed, the mechanical response of the surrounding rock formation and rubble pile are coupled. One cannot exclusively focus on one while ignoring the other. Furthermore, one cannot experimentally characterize a rubble pile's mechanical and hydraulic behavior while it reconsolidates–the rubble pieces are simply too large to be tested in a laboratory. This limitation caused us to try to explicitly model the rubble pieces within the rubble pile, and eventually validate the model predictions against tests on smaller, laboratory-sized, samples. This approach, of course, assumes the model will properly capture size effects. Before validation can begin, however, one must demonstrate a modeling capability, and many conventional geomechanical numerical methods struggle to simulate the fracture, severe deformations, pervasive contact, and healing that occur during room collapse and reconsolidation.

After surveying several numerical methods, we

elected to pursue meshless methods, which combine some of the advantages of particle methods and continuum methods. Similar to particle methods, materials can sustain severe deformations and neighboring material points can separate (fracture) without deleting material (elements). Similar to continuum methods, the strain or strain increment at a material point can be computed using shape functions, meaning meshless methods can use classical continuum-level material models. Meshless methods, of course, are not without drawbacks. For example, surfaces are typically implicitly represented as "mushy" boundaries rather than explicit discontinuities, which makes classical friction models difficult to implement. In addition, meshless run times are often reported to be longer than equivalently resolved continuum methods. Three meshless methods were selected as potentially suitable for room collapse and reconsolidation: the Reproducing Kernel Particle Method (RKPM) (Chen et al., 1996), the Conformal Reproducing Kernel (CRK) method (Koester and Chen, 2019), and the Immersed Isogeometric Analysis (IGA) Meshfree method (Bazilevs et al., 2017b; Bazilevs et al., 2017a).

The remainder of this paper is organized as follows. The salt material model, initial boundary value problem, and the meshless methods are described in Section 2. The results from the meshless simulations are presented in Section 3. Further analysis of the results is discussed in Section 4, and Section 5 concludes with a summary.

## 2 MODEL SETUP AND NUMERICAL METHODS

### *2.1 Salt Material Model*

The salt behavior was simulated using an isotropic, hyperelastic, viscoplastic, continuum damage, model. The material model was designed to capture the essential physical processes, yet remain relatively simple for numerical method assessment. The following presentation follows the geomechanics convention that compressive stresses are positive and tensile stresses are negative.

Continuum damage models distinguish between a macroscopic stress tensor $\boldsymbol{\sigma}$, which is used by the momentum balance equations, and a Kachanov stress tensor $\hat{\boldsymbol{\sigma}}$, which is usually only utilized inside the material model (Kachanov, 2013). This model decomposes $\boldsymbol{\sigma}$ into principal stresses $\sigma_i$ and principal stress directions $\boldsymbol{e}_i$ as

$$\boldsymbol{\sigma} = \sum_{i=1}^{3} \sigma_i \, \boldsymbol{e}_i \otimes \boldsymbol{e}_i. \tag{1}$$

In this principal stress form, one can then define the Kachanov stress as

$$\hat{\boldsymbol{\sigma}} = \sum_{i=1}^{3} \frac{\sigma_i}{1-\omega_i} \, \boldsymbol{e}_i \otimes \boldsymbol{e}_i, \tag{2}$$

where $0 \leq \omega_i \leq 1$ is the principal damage corresponding to principal stress $\sigma_i$. All three principal damages are equal, unless one or more have exceeded the tensile damage limit $\omega^{\mathrm{t}}$ or the compressive damage limit $\omega^{\mathrm{c}}$:

$$\omega_i = \begin{cases} \min(\omega, \, \omega^{\mathrm{t}}), & \text{for } \sigma_i < 0 \\ \min(\omega, \, \omega^{\mathrm{c}}), & \text{for } \sigma_i \geq 0 \end{cases}, \tag{3}$$

where $\omega$ is the isotropic damage variable when a tensile or compressive limit is not active. This formulation allows the material to reach complete tensile failure while still retaining some resistance to compressive stresses.

The model decomposes the total strain rate $\dot{\boldsymbol{\varepsilon}}$ into an elastic strain rate $\dot{\boldsymbol{\varepsilon}}^{\mathrm{el}}$ and a viscoplastic strain rate $\dot{\boldsymbol{\varepsilon}}^{\mathrm{vp}}$:

$$\dot{\boldsymbol{\varepsilon}} = \dot{\boldsymbol{\varepsilon}}^{\mathrm{el}} + \dot{\boldsymbol{\varepsilon}}^{\mathrm{vp}}. \tag{4}$$

Dilation strain associated with damage is neglected for simplicity. The elastic behavior utilizes generalized Hooke's law in rate form, which is the following linear relationship between the elastic strain rate $\dot{\boldsymbol{\varepsilon}}^{\mathrm{el}}$ and the stress rate $\dot{\boldsymbol{\sigma}}$,

$$\dot{\boldsymbol{\sigma}} = \boldsymbol{\mathcal{C}} : \dot{\varepsilon}^{\mathrm{el}}, \tag{5}$$

$$\boldsymbol{\mathcal{C}} = (B - 2/3\,\mu)\, \boldsymbol{I} \otimes \boldsymbol{I} + 2\,\mu\, \boldsymbol{\mathcal{I}}, \tag{6}$$

where $\boldsymbol{\mathcal{C}}$ is the fourth-order elastic stiffness tensor composed of the bulk modulus $B$, the shear modulus $\mu$, the second-order identity tensor $\boldsymbol{I}$, and the fourth-order symmetric identity tensor $\boldsymbol{\mathcal{I}}$. Damage likely reduces the elastic stiffness tensor, but this effect was ignored for simplicity.

The model utilizes the von Mises stress as its equivalent Kachanov shear stress measure, defined as

$$\hat{\bar{\sigma}} = \sqrt{\tfrac{3}{2}\, \hat{\boldsymbol{\sigma}}^{\mathrm{dev}} : \hat{\boldsymbol{\sigma}}^{\mathrm{dev}}} \tag{7}$$

where $\hat{\boldsymbol{\sigma}}^{\mathrm{dev}} = \hat{\boldsymbol{\sigma}} - \hat{p}\, \boldsymbol{I}$ is the deviatoric Kachanov stress tensor and $\hat{p} = \mathrm{tr}(\hat{\boldsymbol{\sigma}})/3$ is the Kachanov pressure. The viscoplastic strain evolves according to an associated flow rule

$$\dot{\boldsymbol{\varepsilon}}^{\mathrm{vp}} = \dot{\bar{\varepsilon}}^{\mathrm{vp}} \frac{\partial \hat{\bar{\sigma}}}{\partial \hat{\boldsymbol{\sigma}}}, \tag{8}$$

where $\dot{\bar{\varepsilon}}^{\mathrm{vp}}$ is the equivalent viscoplastic strain rate. For simplicity, the model neglects transient creep

and includes only steady-state creep. The evolution equation for the equivalent viscoplastic strain involves two terms:

$$\dot{\bar{\varepsilon}}^{\mathrm{vp}} = \sum_{i=1}^{2} A_i \left( \frac{\hat{\bar{\sigma}}}{\mu} \right)^{n_i} \tag{9}$$

where the variables $A_i$ and $n_i$ are model parameters and $\bar{\varepsilon}^{\mathrm{vp}}$ is initialized to zero.

Many salt models employ the concept of a dilatancy boundary (see, for example, Chan et al., 1998; Günther and Salzer, 2012; Hampel, 2015). This model includes damage, but neglects dilation for simplicity, so the dilatancy boundary is referred to as the damage boundary. The damage boundary has the following Drucker-Prager form,

$$\hat{\bar{\sigma}}^{\mathrm{db}} = B_2 \left( \hat{p} - B_1 \right), \tag{10}$$

where $B_1$ and $B_2$ are model parameters.

The damage evolution equation is

$$\dot{\omega} = \frac{D}{\mu} \left\langle \hat{\bar{\sigma}} - \hat{\bar{\sigma}}^{\mathrm{db}} \right\rangle \left( \dot{\bar{\varepsilon}}^{\mathrm{vp}} + \alpha \, \dot{\bar{\varepsilon}}^{\mathrm{el}} \right), \tag{11}$$

where $\omega$ is initialized at zero for intact salt and $\dot{\bar{\varepsilon}}^{\mathrm{el}} = \sqrt{\dot{\boldsymbol{\varepsilon}}^{\mathrm{el}} : \dot{\boldsymbol{\varepsilon}}^{\mathrm{el}}}$. The quantities $D$ and $\alpha$ are material parameters. Damage can only evolve if $\hat{\bar{\sigma}}$ is above $\hat{\bar{\sigma}}^{\mathrm{db}}$, as reflected by the Macaulay bracket factor $\left\langle \hat{\bar{\sigma}} - \hat{\bar{\sigma}}^{\mathrm{db}} \right\rangle$. Note that the $\alpha \, \dot{\bar{\varepsilon}}^{\mathrm{el}}$ term was added as a simple way to make the material more brittle.

Cracks in salt heal under high confining pressures and low deviatoric stresses. The model neglects healing because salt inside the rubble pile that begins to heal is unlikely to subsequently damage and fracture again.

Table 1: Salt model parameter values.

| Type | Parameter | Units | Value |
|---|---|---|---|
| Elastic | $\mu$ | GPa | 12.4 |
| | $B$ | GPa | 20.7 |
| Viscoplastic | $A_1$ | $\mathrm{s}^{-1}$ | $2.154 \times 10^{-6}$ |
| | $n_1$ | – | 1.595 |
| | $A_2$ | $\mathrm{s}^{-1}$ | $1.693 \times 10^{9}$ |
| | $n_2$ | – | 6.279 |
| Damage | $B_1$ | MPa | -2.0 |
| | $B_2$ | – | 1.0 |
| | $D$ | – | $5 \times 10^{4}$ |
| | $\alpha$ | – | 2.0 |
| | $\omega^{\mathrm{t}}$ | – | 0.999999 |
| | $\omega^{\mathrm{c}}$ | – | 0.5 |

The parameter values for the material model were selected using engineering judgement, and they are listed in Table 1. Accurate numerical predictions of room collapse and rubble pile consolidation will eventually require higher quality parameter selection methods, but the parameters in Table 1 should suffice for the numerical method assessment pursued herein.

## 2.2 *Geometry and Boundary Conditions*

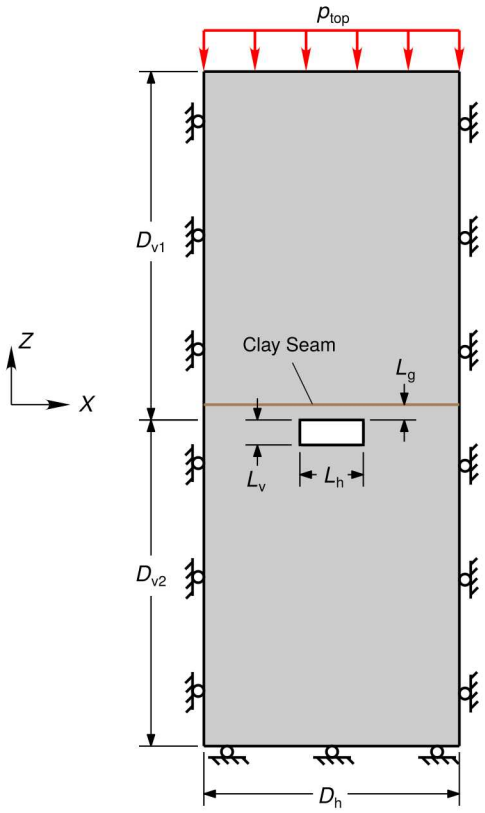


Figure 2: Geometry and boundary conditions.

Figure 2 depicts the geometry and boundary conditions used in the assessment problem. This setup was chosen to resemble the closure of the room in Fig. 1a, except the stratigraphy was simplified to pure salt. The boundary conditions involved rollers on three sides and a normal pressure of $p_{\mathrm{top}} = 13.57$ MPa at the top. The disposal room's 91.44 m length in the $Y$-direction (into the page) was assumed to be long enough relative to the height and width of the room to be treated as plane strain. Each disposal panel at the WIPP consists of seven rooms placed 40.54 m apart, east to west. Here, the seven disposal rooms were treated as if they were an infinite array, such that only one disposal room with mirror boundary conditions $D_{\mathrm{h}} = 40.54$ m apart needed to be modeled. The room ceiling was $D_{\mathrm{v1}} = 55.30$ m and $D_{\mathrm{v2}} = 51.76$ m from the top and bottom of the simulated domain, respectively. Any gas within the room was allowed to escape without providing back pressure as the room closed. The as-excavated room width and height were $L_{\mathrm{h}} = 10.06$ m

and $L_v = 3.96$ m, respectively. A 0.2 m thick clay seam, whose mid-thickness was $L_g = 2.43$ m above the room ceiling, was modeled as salt with an initial damage of $\omega = 0.9$ to reflect the lower strength of the clay seam relative to the neighboring salt. As mentioned in Section 1, friction models are not trivial to implement in meshless methods, so sliding contact between salt surfaces was assumed to be frictionless.

### *2.3 Numerical Methods*

Although meshless methods have been under development for decades, they are somewhat novel to the rock mechanics community. Thus, we briefly introduce each method as we specify the actual approach utilized by a given method.

The RKPM uses the Galerkin approach for solving partial differential equations, similar to the Finite Element (FE) method. Where the FE method requires a mesh to define approximation functions, RKPM only requires a cloud of points. The meshfree approximants avoid mesh distortion or entanglement which are problematic for FE method when simulating large deformations and fragmentation (Chen et al., 1996; Chen et al., 2017; Huang et al., 2020). Herein, a semi-Lagrangian formulation is used where node neighbors and approximants are periodically updated, providing additional fidelity and robustness at extreme deformations. For effective numerical integration, the variationally consistent naturally stabilized nodal integration (VC-NSNI) (Chen et al., 2013) is employed. The low energy modes are suppressed by introducing an implicit gradient type regularization (Hillman and Chen, 2016). A pressure projection technique is used to handle salt's nearly incompressible deformation. Finally, the reproducing kernel strain regularization method (RKSR, Chen et al., 2004) provides discretization-independent and convergent computations of material damage and separation.

The CRK method is a variant of RKPM where approximation functions are modified to better handle domain boundaries and material interfaces (Koester and Chen, 2019). A total Lagrangian formulation is used and the nearly incompressible behavior of salt is handled with an $\bar{\boldsymbol{F}}$ approach recently developed in Moutsanidis et al., 2019.

The Immersed IGA Meshfree Method was proposed and developed in Bazilevs et al., 2017b; Bazilevs et al., 2017a, for air-blast fluid-structure interaction (FSI) applications. The framework makes use of two discretizations, referred to as background and foreground meshes or grids. The fixed background Eulerian grid provides the basis functions for the approximation of the solution of the governing differential equations in the weak form. In the absence of a fluid (or gas), as in the present application, only the equations of solid mechanics are solved using the background mesh, which makes the resulting numerical formulation similar to the well-known material-point method (MPM, Sulsky et al., 1994). The foreground grid is a collection of Lagrangian material points that move through the background grid. One distinguishing feature of the IGA approach is the smooth (i.e., higher-order continuous) B-Spline functions for the background discretization. This additional smoothness renders the strain-rate approximation continuous across the elements of the background mesh, which naturally removes the well-known cell-crossing instability of classical MPM. Finally, to address the nearly incompressible nature of the viscoplastic deformations of the salt, the $\bar{\boldsymbol{F}}$ approach developed in Moutsanidis et al., 2019, was used.

All three meshless method implementations investigated herein explicitly integrate the momentum balance equations. Explicit time integration requires a very small maximum time step $\Delta t^{\text{mb}}_{\text{max}}$, often on the order of 10 μs, for numerical stability. This makes explicit time integration well suited to simulating short duration events, such as car crashes, but anything that lasts longer than a few seconds usually is not practical. To enable longer term simulations using explicit time integration, the salt's viscoplastic strain rate was scaled up to squeeze hundreds of years into a few momentum balance seconds. If we define the physical time as $t$ and the momentum balance time utilized by the explicit time integration algorithm as $t^{\text{mb}}$, then the viscoplastic scale factor $s = s(t^{\text{mb}})$ is

$$s = \frac{\dfrac{\mathrm{d}\bar{\varepsilon}^{\text{vp}}}{\mathrm{d}t^{\text{mb}}}}{\dfrac{\mathrm{d}\bar{\varepsilon}^{\text{vp}}}{\mathrm{d}t}} = \frac{\mathrm{d}t}{\mathrm{d}t^{\text{mb}}}. \tag{12}$$

This scale factor $s$ was progressively scaled up to avoid inertial effects during the beginning of the simulations, yet still reach full reconsolidation in reasonable run times. Further details of the viscoplastic strain rate scaling and other numerical details can be found in Reedlunn et al., 2019.

## 3 SIMULATION RESULTS

### *3.1 Room Closure Without Damage*

Before proceeding to the full room collapse and reconsolidation problem described in Section 2, the three meshless methods simulated a room closure problem without damage. In this problem, damage

evolution was prohibited ($D = 0$) and the clay seam in Fig. 2 was removed, such that closure was solely due to salt viscoplasticity. Sandia also ran this room closure problem with the FE method in Sierra/Solid Mechanics, 2019, to provide a reference solution to compare against. A small study demonstrated that the reference solution quantities of interest had converged with FE mesh refinement.

To quantitatively compare simulation results, it is helpful to define the relative porosity $\phi/\phi_0$. The current porosity is defined as $\phi = V/V_{\text{enc}}$, where $V$ is the current void volume and $V_{\text{enc}}$ is a fixed Eulerian volume that fully encloses $V$. The original porosity is defined as $\phi_0 = V_0/V_{\text{enc}}$, where $V_0$ is the original void volume. Thus, the relative porosity is $\phi/\phi_0 = V/V_0$.

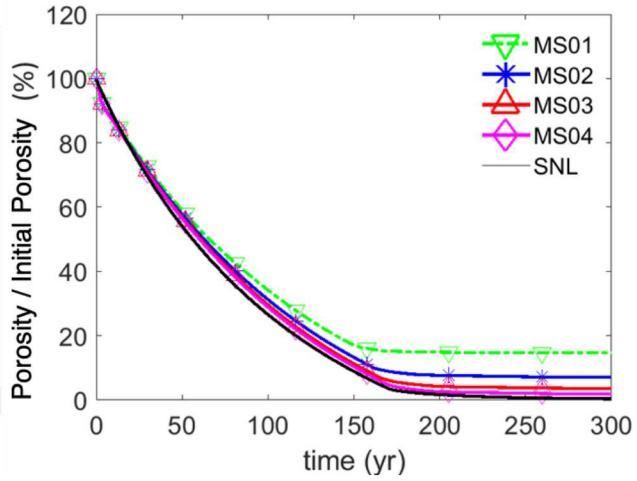


Figure 3: Gradual room closure relative porosity histories. Discretization convergence of RKPM predictions (MS01, MS02, MS03, and MS04) compared against a mesh converged FE method prediction (SNL).

All three meshless methods successfully capture the closure of a room without damage. The simulations labeled MS01, MS02, MS03, and MS04 in Fig. 3 correspond to RKPM simulations with minimum nodal spacings of 0.4 m, 0.2 m, 0.1 m, and 0.05 m, respectively. As the RKPM discretization is refined, the relative porosity histories converge to the FE reference solution. Similar results were found for the Immersed IGA Meshfree method. The CRK simulations also converged to the FE reference solution, but convergence required less discretization refinement than the other two methods because the CRK method utilizes an (approximate) explicit surface representation, rather than an implicit surface representation (Reedlunn et al., 2019).

The room closure problem without damage was also used to assess the computational efficiency of the three methods. The comparison between the CRK and FE methods is perhaps the most relevant, as CRK shares much of the same underlying architecture as the FE method in Sierra/Solid Mechanics, 2019, while the other two meshless methods each have their own architecture. Table 2 lists the maximum stable momentum balance time step size $\Delta t^{\text{mb}}_{\text{max}}$, run time per time step $\Delta t^{\text{run}}$, and run time per momentum balance time step size $\Delta t^{\text{run}} \,/\, \Delta t^{\text{mb}}$ for a CRK simulation with a 1.6 support size and a FE method simulation using the selective deviatoric element with the same nodal discretization. Although $\Delta t^{\text{run}}$ is about 2× bigger for the CRK method than the FE method, $\Delta t^{\text{mb}}_{\text{max}}$ was also about 2× larger for the CRK method, resulting in comparable values of $\Delta t^{\text{run}} \,/\, \Delta t^{\text{mb}}$. In other words, the CRK simulation had about the same run time as the FE simulation.

| Method | $\Delta t^{\text{mb}}_{\text{max}}$ (s) | $\Delta t^{\text{run}}$ (s) | $\frac{\Delta t^{\text{run}}}{\Delta t^{\text{mb}}}$ (s/s) |
|---|---|---|---|
| CRK | 7.226e-05 | 0.907 | 11768.5 |
| FE | 3.418e-05 | 0.473 | 11198.5 |

Table 2: Comparison of CRK and FE method computational performance.

### *3.2 Room Collapse and Reconsolidation*

Both the RKPM and the Immersed IGA Meshfree method were found to be well suited to simulating the room collapse and reconsolidation problem defined in Section 2. Neither method exhibited a significant advantage, so this section will focus on the RKPM results. A fracture methodology for the CRK method is still under development, so the CRK method was not used to simulate room collapse and reconsolidation.

Figure 4 depicts the damage fields during the room collapse and reconsolidation simulation. At $t = 0$ yr, the room has just been excavated, yet damage bands at $\pm 45°$ to the room walls are already emanating from the room corners. By $t = 7$ yr, the bands are more intense and extend above and below the room, making angles of $\pm 45°$ with the room ceiling and floor. The bands above the room intersect the clay seam, cutting out a trapezoidal shaped block. During the seventh year, this trapezoidal block falls into the room, lands on the floor, and breaks into three pieces. Two triangular shaped blocks also break off from the room walls during the seventh year. No further roof falls occur during the rest of the simulation, presumably because the room ceiling has an arch-like shape, which distributes the stress more evenly. Between $t = 7$ yr and $t = 37$ yr,

the enlarged room closes in on the rubble pile while rearranging grinding up the rubble pieces. The closure process is complete by $t = 37$ yr. Note that RKPM handled the severe deformations, fracturing, and extensive contact within the rubble pile with ease.

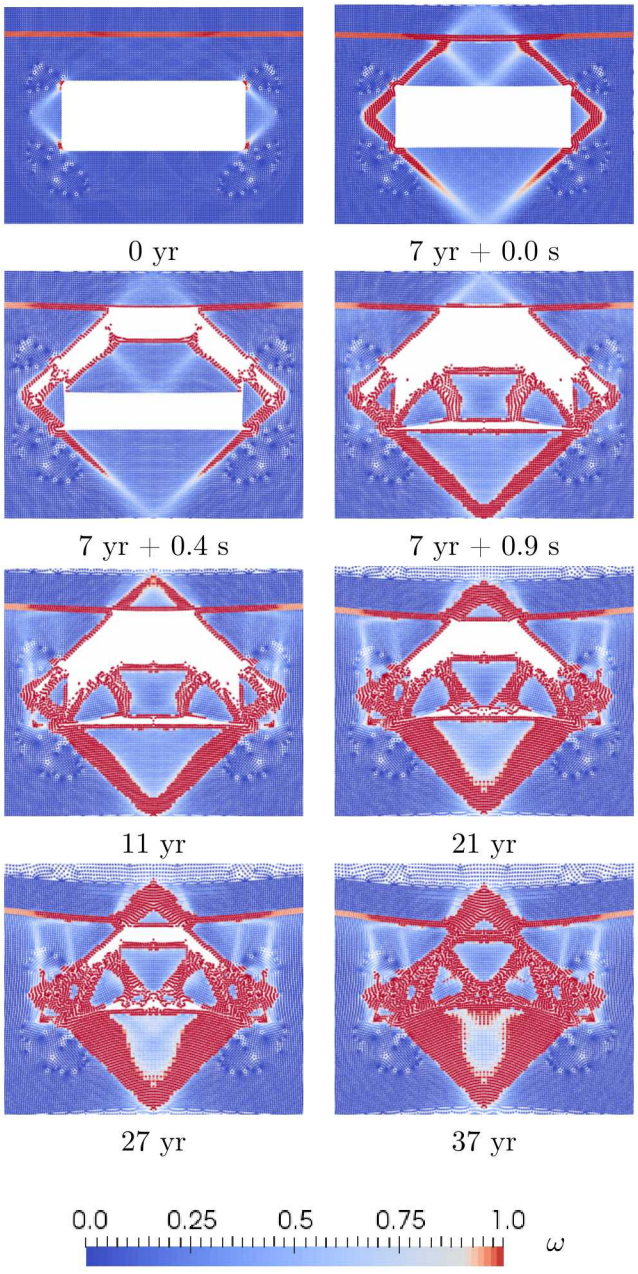


Figure 4: RKPM predicted damage fields during the room collapse and reconsolidation process for $\alpha = 2$.

The relative porosity history during this process is shown in Fig. 5 for several values of the brittleness parameter $\alpha$. The small drop in $\phi/\phi_0$ at $t = 7$ yr coincides with the roof fall, but the underlying cause is still under investigation. After the roof fall, the relative porosity decreases in a nearly linear fashion for the next 30 years, reaching its final value of $\phi/\phi_0 = 4$ % at $t \approx 37$ yr. If the discretization were refined, we expect the final relative porosity to asymptotically approach zero, given the trend in Fig. 3.

Figure 5 also shows that the relative porosity curves are not particularly sensitive to $\alpha$, but this appears to be situation dependent. Another room collapse and reconsolidation simulation, where the clay seam was ignored, was more sensitive to $\alpha$ once the roof fall landed and broke up into rubble (see Figure 4-21 in (Reedlunn et al., 2019)). If the situations of interest at the WIPP continue to be dependent on salt's brittleness, then it may be worthwhile to improve the material model's predictions of high strain rate behavior.

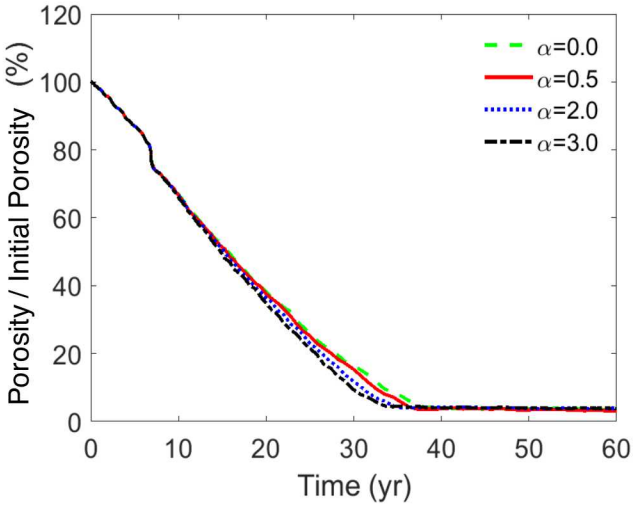


Figure 5: RKPM predicted relative porosity histories during room collapse and reconsolidation for several values of $\alpha$.

## 4 FURTHER ANALYSIS

The meshless simulations in Section 3 predict room closure without damage requires 170 yr, while room collapse and reconsolidation can complete in as little as 37 yr. We can certainly propose model improvements, such as adding friction and healing, that should increase the collapse and reconsolidation time beyond 37 yr, but no mechanisms have been proposed to cause room collapse and reconsolidation to occur more quickly than room closure without damage. In fact, Section 1 presented two mechanisms that cause just the opposite effect: a circular cross-section room viscoplastically closes more slowly than a rectangular cross-section room, and rubble slows down room closure by supplying back pressure. The enlargement of the room as it collapses, however, provides a mechanism for collapsing rooms to close faster than damage-free rooms.

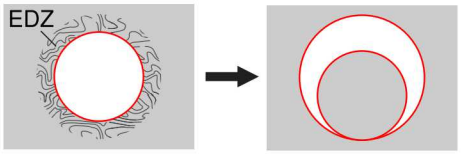


(a) Idealization

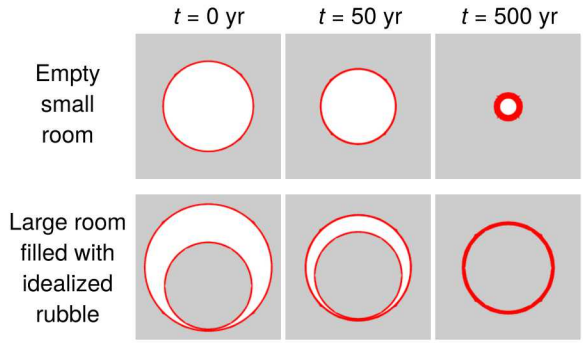


(b) Deformed room shapes at selected times

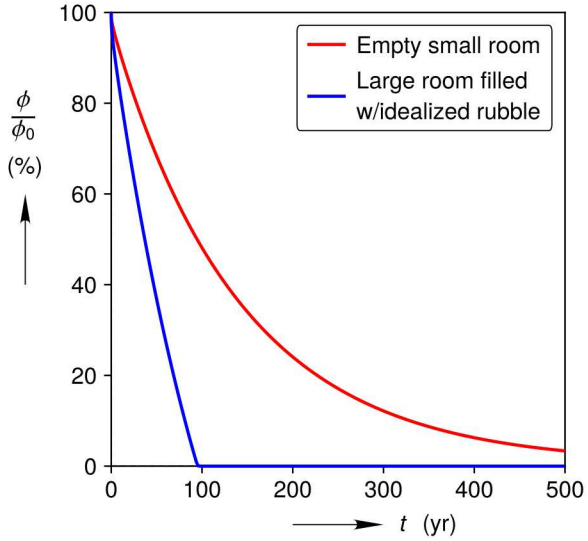


(c) Relative porosity histories

Figure 6: Gradual closure of an empty small room compared against a large room filled with idealized rubble.

The following "toy" problems are used to demonstrate how room enlargement can speed up closure. Take an empty, long, slender, and isolated circular cross-section room, rimmed with an EDZ whose volume is equal to the initial void volume of the room, as shown on the left of Fig. 6a. If one assumes the EDZ cannot sustain any deviatoric stress, forms a rubble pile in the room, and provides zero back pressure until it has fully reconsolidated, then one can increase the room size to the extent of the EDZ and represent the rubble pile as a cylinder of intact salt, as shown on the right of Fig. 6a. The damage-free closure of a small empty room, can then be compared against that of a large room filled with idealized rubble, where both rooms have the same initial void volume $V_0$. The salt viscoplasticity in both toy problems was captured using the Munson-Dawson model, any gases within the room were allowed to escape without supplying back pressure, and the simulations were run using the FE method in Sierra/Solid Mechanics, 2019. See Appendices A.1 and A.2 of Reedlunn et al., 2019 for further details of the model setup and numerical settings.

Enlarging the room, while holding the initial void volume constant, dramatically shortens the time to close a room. Figure 6b presents the room cross-sections at $t = 0$, 50, and 500 yr, where the layer of finite elements closest to the room and surrounding the idealized rubble has been colored red, and Fig. 6c depicts the relative porosity histories. The surface of the large room contacts the idealized rubble at $t = 95$ yr, at which point the relative porosity is zero, while the small room remains open even after 500 yr. Although the rooms are constrained to have the same $V_0$, the large room loses void volume $V$ faster than the small room.

## 5 CONCLUSIONS

The WIPP's long-term waste isolation performance significantly depends on the permeability and porosity of rooms as they close. Sandia has models for rooms filled with nuclear waste containers or crushed salt, but models do not exist for empty room closure. The tendency of empty rooms to collapse and the subsequent rubble pile compaction poses difficult challenges for the prediction of an empty room's permeability and porosity. Nevertheless, Sandia is beginning to simulate the room collapse and reconsolidation processes using meshless methods.

The Immersed IGA Meshfree method, RKPM, and CRK method all appear well suited to model a simplified two-dimensional representation of room closure. First, all three methods accurately and efficiently simulated gradual room closure. Second, the Immersed IGA Meshfree method and RKPM simulated room collapse and reconsolidation. The methods both handled the severe deformations, pervasive contact, and fracturing processes without issues. Interestingly, the methods predicted a collapsing and reconsolidating room closes faster than a damage-free room, which runs counter to two proposed mechanisms that should slow down room collapse and reconsolidation. Further analysis revealed a previously neglected mechanism that acts to speed up the collapse and reconsolidation process.

This project is still in its early stages and has many areas for improvement. Future efforts will improve the salt material model, push the computations into three-dimensions, and begin to compare predictions against laboratory and in-situ observations.

## ACKNOWLEDGEMENTS

Sandia National Laboratories is a multimission laboratory managed and operated by National Technology and Engineering Solutions of Sandia, LLC., a wholly owned subsidiary of Honeywell International, Inc., for the U.S. Department of Energy's National Nuclear Security Administration under contract DE-NA-0003525. This research is funded by WIPP programs administered by the Office of Environmental Management (EM) of the U.S. Department of Energy. SAND2020-XXXX.

## REFERENCES

Bazilevs, Y., Moutsanidis, G., Bueno, J., Kamran, K., Kamensky, D., Hillman, M. C., Gomez, H., and Chen, J. 2017a. "A new formulation for air-blast fluid–structure interaction using an immersed approach: part II—coupling of IGA and meshfree discretizations". In: *Computational mechanics* 60.1, pp. 101–116.

Bazilevs, Y., Moutsanidis, G., Bueno, J., Kamran, K., Kamensky, D., Hillman, M. C., Gomez, H., and Chen, J. 2017b. "A new formulation for air-blast fluid–structure interaction using an immersed approach. Part I: basic methodology and FEM-based simulations". In: *Computational mechanics* 60.1, pp. 101–116.

Camphouse, R. C., Gross, M., Herrick, C., Kicker, D., and Thompson, B. May 2012. *Recommendations and justifications of parameter values for the run-of-mine salt panel closure system design modeled in the PCS-2012 PA*. Memorandum.

Carrasco, R. Sept. 2019a. *Empty areas at the Waste Isolation Pilot Plant*. Personal Communication.

Carrasco, R. Sept. 2019b. *Roof fall photographs*. Personal Communication.

Chan, K. S., Munson, D., Fossum, A., and Bodner, S. 1998. "A constitutive model for representing coupled creep, fracture, and healing in rock salt". In: *Proc. 4th conference on the mechanical behavior of salt*. Ed. by M. Aubertin and H. R. H. Jr. Trans Tech Publications, pp. 221–234.

Chen, J.-S., Hillman, M., and Chi, S.-W. 2017. "Meshfree methods: progress made after 20 years". In: *Journal of engineering mechanics* 143.4.

Chen, J.-S., Hillman, M., and Rüter, M. 2013. "An arbitrary order variationally consistent integration for Galerkin meshfree methods". In: *International journal for numerical methods in engineering* 95.5, pp. 387–418.

Chen, J.-S., Pan, C., Wu, C.-T., and Liu, W. K. 1996. "Reproducing Kernel Particle Methods for large deformation analysis of non-linear structures". In: *Computer methods in applied mechanics and engineering* 139.1-4, pp. 195–227.

Chen, J.-S., Zhang, X., and Belytschko, T. 2004. "An implicit gradient model by a reproducing kernel strain regularization in strain localization problems". In: *Computer methods in applied mechanics and engineering* 193.27-29, pp. 2827–2844.

Günther, R. and Salzer, K. 2012. "Advanced strain-hardening approach: a powerful creep model for rock salt with dilatancy, strength and healing". In: *Proc. 7th conference on the mechanical behavior of salt*. Ed. by P. Bérest, M. Ghoreychi, F. Hadj-Hassen, and M. Tijani. CRC Press/Balkema, pp. 13–22.

Hampel, A. 2015. "Description of damage reduction and healing with the CDM constitutive model for the thermo-mechanical behavior of rock salt". In: *Proc. 8th conference on the mechanical behavior of salt*. Ed. by L. Roberts, K. Mellegard, and F. D. Hansen, pp. 361–371.

Hillman, M. and Chen, J.-S. 2016. "An accelerated, convergent, and stable nodal integration in Galerkin meshfree methods for linear and nonlinear mechanics". In: *International journal for numerical methods in engineering* 107.7, pp. 603–630.

Huang, T.-H., Wei, H., Chen, J.-S., and Hillman, M. C. 2020. "Rkpm2d: an open-source implementation of nodally integrated reproducing kernel particle method for solving partial differential equations". In: *Computational particle mechanics* 7, pp. 393–433.

Kachanov, L. 2013. *Introduction to continuum damage mechanics*. Vol. 10. Springer Science & Business Media.

Koester, J. J. and Chen, J.-S. 2019. "Conforming window functions for meshfree methods". In: *Computer methods in applied mechanics and engineering* 347, pp. 588–621.

Moutsanidis, G., Koester, J. J., Tupek, M. R., Chen, J.-S., and Bazilevs, Y. 2019. "Treatment of near-incompressibility in meshfree and immersed-particle methods". In: *Computational particle mechanics*, pp. 1–19.

Reedlunn, B., Moutsanidis, G., Baek, J., Huang, T.-H., Koester, J., Matteo, E., He, X., Taneja, K., Wei, H., Bazilevs, Y., Chen, J.-S., Mitchell, C., Lander, R., and Dewers, T. Dec. 2019. *Initial simulations of empty room collapse and reconsolidation at the waste isolation pilot plant*. Tech.

rep. SAND2019-15351. Sandia National Laboratories.

Sierra/Solid Mechanics 2019. *Sierra/Solid Mechanics User's Guide*. 4.52. SAND2019-2715. Sandia National Laboratories. Albuquerque, NM, USA; Livermore, CA, USA.

Stone, C. M. Aug. 1997. *Final disposal room structural response calculations*. Tech. rep. SAND97-0795. Albuquerque, NM, USA; Livermore, CA, USA: Sandia National Laboratories.

Sulsky, D., Chen, Z., and Schreyer, H. L. 1994. "A particle method for history-dependent materials". In: *Computer methods in applied mechanics and engineering* 118.1-2, pp. 179–196.